Research Paper
Computational Methods for Differential Equations
http://cmde.tabrizu.ac.ir
Vol. *, No. *, *, pp. 1-24
DOI:10.22034/cmde.2025.62082.2710

Numerical and artificial neural network model for Williamson fluid flow over a stretching sheet under inclined magnetic field and radiation

P. Priyadharshini* **and V. Karpagam**
Department of Mathematics, PSG College of Arts and Science, Coimbatore-641014, Tamil Nadu, India.

Abstract

Potential developments of Williamson fluid flow across porous media included plasma mechanics, blood transport, bio-thermal engineering, medication delivery, and tissue temperature perception. The benefits of these results are evident in the biomedical fields of tissue engineering and tissue replacement, where porous scaffolds improve blood flow across biological tissues and address organ shortages. In the fluid flow model, velocity $U_w(x) = ax$ is influenced by an inclined magnetic field and radiation effect at an angle of α over the stretching surface, with the temperature, concentration, and velocity slips present. Relevant partial differential equations were transformed into ordinary differential equations by the conversion of similarity. The MATLAB module implements the BVP4C solver computationally to determine these ODEs. The current discoveries constitute a remarkable extension of previous results. As the magnetic parameter rises, the Lorentz force acting on the fluid flow reduces the velocity distribution. The temperature profile minimized as the Prandtl number improved because of a reduction in the thickness of the thermal boundary layer. In addition, the proposed innovative work for a machine learning-based multiple linear regression improves the accuracy to 95%. In the end, employing an artificial neural network technique yields highly dependable validation and 99% correct forecasts for such scenarios by locating accurate data for amounts of interest. The exact quality of the prediction and verification of the present result is ultimately verified and confirmed by a graph and tabular data for comparison with the prior outcomes.

Keywords. Artificial Neural Network, Inclined Magnetic Field, Multiple Linear Regression, Radiation.
2010 Mathematics Subject Classification. 92B20, 83C50, 62J05, 78A40.

1. Introduction

One of the most crucial non-Newtonian fluids was the Williamson fluid, which has potential advancement in biomedical and industrial applications such as plasma mechanics, blood circulation, bio-thermal engineering, ice cream paste, fruit juices, polymer melts, greases, and crude oil processing. Initially, Williamson et al. [43] in 1929 provided an excellent experiment to verify these ideas and gave a great example formulation for describing the flow of pseudo-plastic fluids. This technique displayed infinite viscosity when the shear rate is stationary and zero viscosity when the shear rate approaches infinity. After that, Lyubimov et al. [19] explored the movement of a tiny layer of Williamson fluid to produce translational vibrations in its plane across an inclined, infinite solid surface. Subsequently, Vasudev et al. [41] examined the Williamson fluid peristaltic pumping over a porous material in a horizontal tube involving thermal transfer. In further study, Nadeem et al. [20] evaluated the impact of Williamson fluid on boundary flow and heat transfer across a stretching surface. Recently, Haider et al. [9] developed a novel heat flux model to investigate the thermal properties of hybrid nano-Williamson fluids. He discovered that the rate of species diffusion in a hybrid nanofluid is noticeably higher than in a mono nanofluid. Navigate to the Williamson fluid model due to the previous result demonstrating the significant influence of the industrial and biological domains.

A porous medium, or porous material, is a substance that contains pores. The monitoring of blood flow and tissue temperature, as well as industrial uses for petroleum resources, crude oil production, and energy storage, are

Received: 12 June 2024 ; Accepted: 10 September 2025.
* Corresponding author. Email: priyadharshinip@psgcas.ac.in.

a few of the biomedical and technical applications of a thorough investigation of porous media. From the beginning, Khan et al. [13] analyzed buoyancy-induced flow with non-Newtonian nanofluid characteristics through a porous vertical stretching surface using the model of a third-grade fluid. He caught the impact of buoyancy. Afterward, Bhatti et al. [2] studied the influence of a magnetic field on the peristaltic behavior of the Williamson fluid utilizing empirical and computational methods. The above results show the impact of the Williamson fluid parameter, the nano-Lewis number, and the Dufour solute Lewis number. Later, Krishna et al. [17] tested the ion slip and Hall ripples affecting the non-Newtonian fluid hydromagnetic convective fluxes through an impermeable medium connected to two gyrating parallel plates for an instant sporadic sinusoidal pressure gradient. Following that, Shamshuddin et al. [32] analyzed magnetohydrodynamics (MHD) bioconvection techniques for microbial nanofluid treatment using permeable surfaces and an induced heat source and tested the size of the motile density of microorganisms damped for different thermophysical factors. Soon after, Usman et al. [40] observed that a semi-numerical method for heat transference in a Williamson fluid moving along a ciliated porosity medium. By looking at the previously mentioned results, this framework facilitates an analysis of the Williamson fluid with a porous surface stretching sheet.

An inclined magnetic field represents a slanted field at an angle rather than precisely aligned with the reference direction, and it has a non-zero inclination. It is crucial for assessing the capabilities of MHD plasma devices, accelerators, and energy systems used in actual geophysical and biological processes. Ramesh et al. [27] addressed the effects of the transmission of heat on magnetohydrodynamics second-grade fluid across the permeable substance in an imbalanced tunnel, and they discussed the contribution of the inclination angle on the flow. Following that, Sreedevi et al. [34] explored the heat and mass distribution of nanofluids on linear and nonlinear stretching surfaces that employ thermal radiation and chemical processes. After that, Elgazery et al. [7] demonstrated that nanofluids flow across a porous, unstable extended surface bordered by a non-uniform heat source/sink. The impact of the inclination angle frequently results in an inclined magnetic field. Koriko et al. [16] investigated the bioconvection flow of an MHD thixotropic nanofluid across a vertical surface with the effects of gyrotactic bacteria and nanoparticles. Rehman et al. [29] examined the impact of the non-Fourier heat flow model, magnetic field, and Darcy-Forchheimer equation on the Casson dusty nanofluid. Rauf et al. [28] evaluated the MHD micropolar non-Newtonian tri-hybrid nanofluid flow between two parallel surfaces, which is affected by Hall current and morphological factors. In addition, Abdelhafez et al. [1] discussed heat and mass transfer with an angled magnetic field, affecting peristaltic blood circulation in an unconventional stream, and their result signifies the shear stress of the blood. Choudhari et al. [5] inspected the effects of numerous slips on MHD plasma peristaltic flow applying Phan-Tien-Tanner nanofluid through an asymmetric route, which influenced blood rheology. After that, Many researchers studied the impact of an angled magnetic field and Williamson fluid flow across porous media ([44], [15],[22], [26], and [4]). After examining the earlier findings, this structure provides a Williamson fluid research using a stretched sheet with an angled magnetic field porous surface.

This study examines the multi-slip and thermal radiation impact of Williamson fluid flow through a stretching sheet in an environment of a highly inclined magnetic field, providing outstanding targets for the previously suggested favorable results of Wang et al. [42], Gorla et al. [8], Khan et al. [14], Srinu et al. [36]. The earlier outcomes indicated that elevating the Prandtl and Weissenberg numbers minimized the temperature distribution and reduced the velocity distribution as the magnetic field rose. It offers advantages in various biomedical fields, including drug administration, heat transmission in biological tissues, and tissue formation using porous scaffolds.

1.1. **Framework.** The current investigation has five parts: mathematical formulation, methodology, discussion of results, validation, and conclusion.

⋆ Formation of mathematical equations is known as flow analysis.

⋆ The numerical technique for solving these equations under appropriate boundary conditions, as executed by the MATLAB module BVP4C solver, demonstrated the solution methodology.

⋆ A summary of the numerical and machine learning studies indicated that prior findings were validated, as described in the results and comments.

⋆ The outcome compared with previous results depicted the validation.

⋆ The outcome displayed in the concluding remarks.

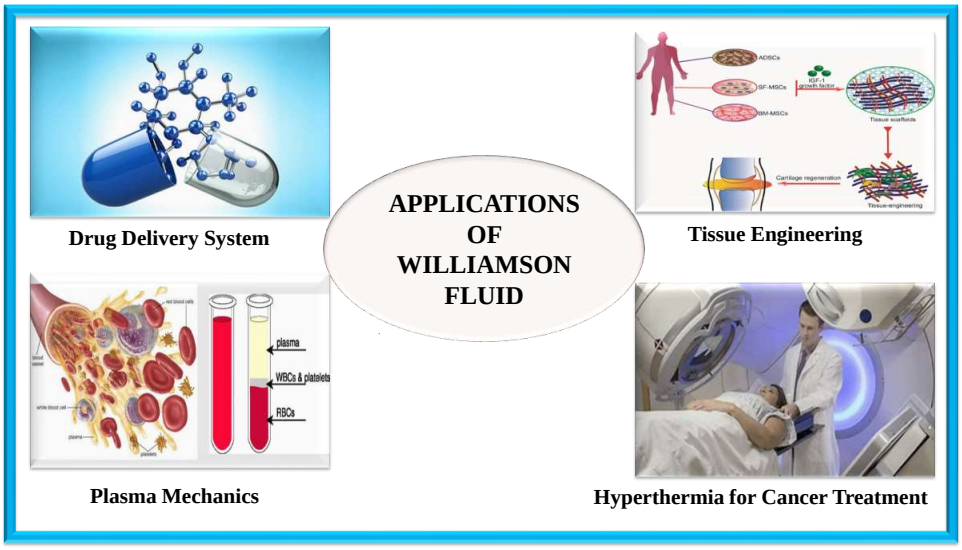

FIGURE 1. Applications of Williamson fluid.

2. Flow Analysis

An angled magnetic field and heat radiation were employed to examine the effects of Williamson fluid flow on a stretching sheet. This experiment looked at a stretching surface with the ambient fluid temperature T_w, the upper part of the surface T_∞, and the velocity $U_w(x) = ax$. The positioning of a flow control provides $y > 0$. The fluid flow is subjected to an orthogonal magnetic field to the x-axis at an angle of α. An estimated difference exists between the applied and induced magnetic fields. Figure 1 indicates the application of Williamson fluid, and Figure 2 illustrates the structure of the geometrical representation.

Srinivasulu et al. [35] and Srinu et al. [36] and address the governing equations of momentum, energy, and concentration.

$$u_x + v_y = 0, \tag{2.1}$$

$$uu_x + vu_y = \nu u_{yy} + \sqrt{2}\nu\Gamma u_y u_{yy} - \frac{\sigma B_0^2}{\rho_f} sin^2(\alpha)u - \frac{\nu}{k^*}u, \tag{2.2}$$

$$uT_x + vT_y = \frac{k}{(\rho c_p)_f}T_{yy} + \frac{1}{(\rho c_p)_f}\frac{16\sigma^* T_\infty^3}{3K^*}T_{yy} + \frac{\sigma B_0^2}{(\rho c_p)_f}u^2 + \frac{\nu}{C_p}\left[u_y^2 + \sqrt{2}\Gamma u_y^3\right] + Q_0(T - T_\infty), \tag{2.3}$$

$$uC_x + vC_y = D_B C_{yy} - Kc^*(C - C_\infty), \tag{2.4}$$

The boundary constraints are:

$$\begin{aligned} &u = u_w = ax + A^* u_y, v = v_w, T = T_w + B^* T_y, C = C_w + C^* C_y \ at \ y \to 0, \\ &u = 0, T \to T_\infty, C \to C_\infty, \ as \ y \to \infty. \end{aligned} \tag{2.5}$$

The stream function is

$$u = \psi_y, v = -\psi_x. \tag{2.6}$$

The system of equations generates the dimensionless flow model to apply the following non-dimensional similarity transformations.

$$\psi = \sqrt{a\nu}xf(\eta), \ \eta = y\sqrt{\frac{a}{\nu}}, \ \theta(\eta) = \frac{T - T_\infty}{T_f - T_\infty}, \ \phi(\eta) = \frac{C - C_\infty}{C_\infty - C_w}. \tag{2.7}$$

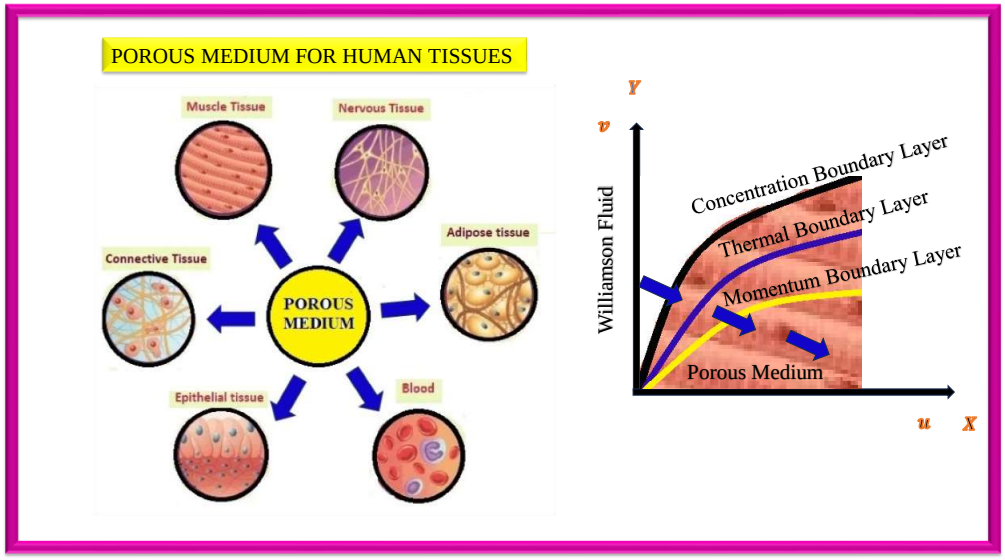

FIGURE 2. Proposed geometrical diagram.

The stream function satisfies continuity Equation (2.1) and generates nonlinear ordinary differential equations by modifying the nonlinear parameters in Equations (2.2)-(2.4) and boundary restrictions in Equation (2.5) are as shown below:

$$\left(1+\lambda f^{''}(\eta)\right) f^{'''}(\eta) + f(\eta) f^{''}(\eta) - (f^{'})^{2}(\eta) - \left(Msin^{2}(\alpha) + K_{p}\right) f^{'}(\eta) = 0, \tag{2.8}$$

$$\theta^{''}(\eta) + \frac{Pr}{(1+R)}\left[f(\eta)\theta^{'}(\eta) + Ec\left((f^{''})^{2}(\eta) + We(f^{''})^{3}(\eta) + M(f^{'})^{2}(\eta)\right) + Q\theta(\eta)\right] = 0, \tag{2.9}$$

$$\phi^{''}(\eta) + Lef(\eta)\phi^{'}(\eta) - LeKc\phi(\eta) = 0. \tag{2.10}$$

The boundary restrictions are

$$\begin{aligned} &f(\eta) = f_{w}(0),\ f^{'}(\eta) = 1 + Af^{''}(0),\ \theta(\eta) = 1 + \delta\theta^{'}(0),\ \phi(\eta) = 1 + \gamma\phi^{'}(0),\ at\ \eta \to 0, \\ &f^{'}(\eta) \to 0,\ \theta(\eta) \to 0,\ \phi(\eta) \to 0,\ as\ \eta \to \infty. \end{aligned} \tag{2.11}$$

The skin friction, Nusselt number, and Sherwood numbers are

$$C_{f_x} = \frac{\tau_w}{\rho u_w^2},\ N_{u_x} = \frac{xq_w}{k(T-T_w)},\ S_{h_x} = \frac{xq_m}{D_B(C_\infty - C_w)}. \tag{2.12}$$

where the shear stress and thermal flux are

$$\tau_w = \mu\left[u_y + \frac{\Gamma}{\sqrt{2}}u_y^3\right],\ q_w = -k(T_y)_{y=0}. \tag{2.13}$$

The dimensionless form of skin friction, Nusselt, and Sherwood values evaluated from Equations (2.7), (2.12), and (2.13).

$$C_{f_x}\sqrt{Re_x} = \left(1 + \frac{\lambda}{2}f^{''}(0)\right) f^{''}(0),\ \frac{N_{u_x}}{\sqrt{Re_x}} = -(1+R)\theta^{'}(0),\ \frac{S_{h_x}}{\sqrt{Re_x}} = -\phi^{'}(0). \tag{2.14}$$

Table 1 exhibits distinguished physical parameters.

TABLE 1. Values for several physical parameters.

S.No	Physical Parameters	Physical Parameter Values
1	Magnetic Parameter	$M = \frac{\sigma B_0^2}{\rho_f a}$
2	Prandtl number	$Pr = \frac{k}{(\rho C_p)_f}$
3	Williamson factor	$\lambda = \sqrt{\frac{2a}{\nu}} ax\Gamma$
4	Radiation parameter	$R = \frac{16\sigma^* T_\infty^3}{3kk^\star}$
5	Suction injection parameter	$f_W = -\frac{\nu_W}{\sqrt{a\nu}}$
6	Weissenberg Number	$We = x\Gamma\sqrt{\frac{2a^3}{\nu}}$
7	Eckert number	$Ec = \frac{U_W^2}{C_P(T_f - T_\infty)}$
8	Lewis number	$Le = \frac{\nu}{D_B}$
9	Chemical reaction parameter	$K_C = \frac{K_C^*}{a}$
10	Reynolds number	$R_{e_x} = \frac{u_w x}{\upsilon}$

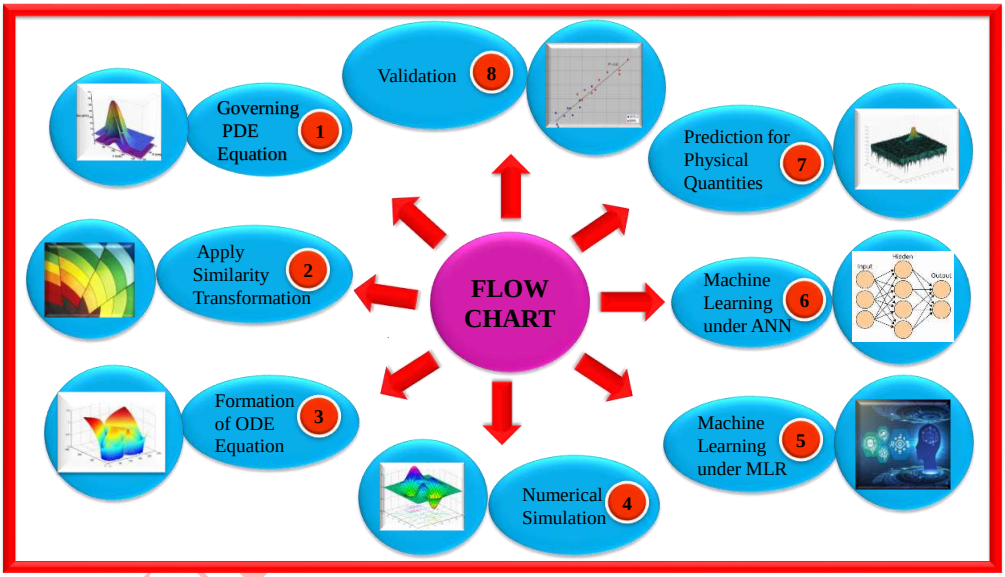

FIGURE 3. Flow chart of proposed approach.

3. Solution Methodology

This research project focuses primarily on numerical and machine-learning methodologies. The main advantage of this approach is that the BVP4C solver MATLAB program reduces higher-order ODEs to first-order ODEs, which is the initial stage in developing a numerical solution. In the second half of the research, multiple linear regression with machine learning enhanced prediction and decision-making processes, resulting in more accurate results. The development of MLR focused on the significant correlation recognized between a single prediction and many response variables. The coefficients corresponding to the different flow conditions that affected each are found and calculated. Finally, precisely predicted and verified the values of physical quantities employing artificial neural networks, yielding results exhibited through mean square error, error histogram, regression, and fitness plots. A simplified flowchart of the recommended method is displayed in Figure 3, emphasizing significant parts of an inquiry.

3.1. **Numerical Approach.** The nonlinear ODE with boundary restrictions are in Equations (2.8)–(2.11) are determined by computationally utilizing MATLAB software, incorporating the BVP4C solution module. For evaluating boundary value problems in ordinary differential equations, Shampine et al. [30] first looked at this solver. Hereafter, Shampine et al. [31] developed this software to solve ordinary differential equations. After that, Dey et al. [6] discovered volume fraction-based two-phase fluid motion in a porous medium. Using this technique, solve thermal radiation on boundary layer flow analyzed by Kamil et al. [12]. A novel numerical technique for calculating Williamson fluid cross-flow over a porous shrinking/stretching surface, combining the hybrid nanofluid and thermal radiation among the finite difference method evaluated by Umair et al. [38].

To introduce the new variables:

$$f(\eta) = y_1, f^{'}(\eta) = y_2, f^{''}(\eta) = y_3, \theta(\eta) = y_4, \theta^{'}(\eta) = y_5, \phi(\eta) = y_6, \phi^{'}(\eta) = y_7. \tag{3.1}$$

The specified variables have transformed from a dimensionless higher-order ODE form to a first-order ODE.

$$y_1^{'} = y_2, \tag{3.2}$$

$$y_2^{'} = y_3, \tag{3.3}$$

$$y_3^{'} = \frac{1}{(1+\lambda y_3)}\left[-y_1 y_3 + y_2^2 + \left(Msin^2(\alpha) + K_p\right) y_2\right], \tag{3.4}$$

$$y_4^{'} = y_5, \tag{3.5}$$

$$y_5^{'} = -\frac{Pr}{(1+R)}\left[y_1 y_5 + Ec\left((y_3)^2 + We(y_3)^3 + M(y_2)^2\right) + Qy_4\right], \tag{3.6}$$

$$y_6^{'} = y_7, \tag{3.7}$$

$$y_7^{'} = -Ley_1 y_7 + LeKcy_6. \tag{3.8}$$

Furthermore, the boundary restrictions:

$$ya_1 = fw, ya_2 = 1 + Aya_3, ya_4 = 1 + \delta ya_5, ya_6 = 1 + \gamma ya_7, yb_2 = 0, yb_4 = 0, yb_6 = 0. \tag{3.9}$$

The BVP4C solver seemed to resolve the system of ODEs and the related boundary requirements are in Equations (3.2)-(3.9).

3.1.1. *Convergence Test for BVP4C Solver.* Integration settings, initial guesses, boundary conditions, step size, and error estimation are vital components in evaluating the convergence of the BVP4C solver. By strategically adjusting the step size, we can achieve highly accurate and dependable results. Our findings demonstrate that expanding the number of intervals significantly minimizes the error. Table 2 shows that setting the number of step sizes to 5 resulted in the highest residual of 7.426e-05, which was solved using an 84-point mesh. However, when increasing the number of step sizes to 50, the solution achieved an 186-point mesh and its optimum residual produced 9.042e-05. Hence, fine-tuning the step size emerges as a critical strategy in the convergence tests for the BVP4C solver. An increment of step size and mesh point enhances resolution by detecting small-scale variations in temperature distribution, resulting in more precise heat transfer analysis in the boundary region.

TABLE 2. Convergence test for BVP4C solver.

Total number of Step Size	**Maximum Residual**	**Number of Mesh**
5	7.426e-05	84
50	9.042e-05	186

3.2. **Machine Learning Approach.**

3.2.1. *Multiple Linear Regression Algorithm.* Artificial intelligence leverages machine learning data to help robots learn, develop new ideas, and perform specialized activities more accurately. It enhances proficiency in applying decision-making and resource evaluation methods to gather relevant data from massive databases to advance fluid mechanics research. Furthermore, this method automatically regulates, optimizes, and raises the flow. Heureux et al. [10] provided extensive details on ML, emphasizing its challenges and techniques. Sulochana et al. [37] investigated the effect of temperature source-sink on classification and regression algorithms that use nanofluid flows on an expanding surface. Palash et al. [21] investigated temperature conductive prediction for titania-water nanofluid using several forecasting machine learning algorithms. The current work employed a multiple linear regression approach to forecast fluid physical parameters, which is consistent with the prevalence of predictive algorithms in the domain ([24]-[25]).

3.2.2. *Structure of MLR.* MLR determines a complex interaction between a single predictor component and several physical quantities. The evidence-based multiple regression evaluation technique aims to discover errors or deviations while also characterizing the final anticipated findings. The implementation of multiple regression techniques to forecast the physical parameter values of skin friction, Nusselt number, and Sherwood number.
The estimation of multiple linear regression utilizes the following formula

$$Y = \alpha_0 + \alpha_1 X_1 + \alpha_2 X_2 + ... + \alpha_n X_n + \epsilon. \tag{3.10}$$

The value of Y is the prediction variable, $X_1, X_2, ..., X_n$ are the response variables, the constant term α_0 depicted as the regression line on the vertical axis, it is denoted by the intercept, $\alpha_1, \alpha_2, ..., \alpha_n$ indicated the regression coefficient and ϵ represented as the random error.

The preceding Equations (3.11)-(3.13) provides the skin friction, Nusselt, and Sherwood numbers.

$$C_{f_x} = 0.94248 + 0.081444 * M + 0.44312 * fw + 0.33659 * Kp - 0.89831 * A, \tag{3.11}$$

$$N_{u_x} = 1.1527 + 0.13677 * Pr - 1.2102 * Ec + 0.16721 * We - 3.2539 * Q - 0.51885 * R - 0.45595 * \delta, \tag{3.12}$$

$$S_{h_x} = 1.3465 + 0.1572 * Le + 0.35224 * Kc - 2.8461 * \gamma. \tag{3.13}$$

3.2.3. *Artificial Neural Network Algorithm.* The conceptual architecture of the human brain serves as a source of inspiration for the working mechanism of machine learning under artificial neural networks (ANN). It is an excellent resource for modeling nonlinear statistical data. The input, output, and hidden layers are the three interconnected layers that make up an artificial neural network. The first layer contains the neurons in the input layer. The final output layer receives the information that those neurons supply to the deeper layers. Through a series of transformations, the hidden units that comprise the inner layers adaptively modify the data they receive layer by layer. A specific artificial neural network model forecasts the hydrodynamic flow characteristics of a Williamson fluid in a stratified environment with a convective surface. Shoaib et al. [33] examined the application of Levenberg-Marquardt backpropagation neural networks to intelligent computing for third-grade nanofluid on a stretched sheet under convective conditions. Ullah et al. [39] investigated the backpropagation neural networks in the Levenberg-Marquard algorithm for ANN in the numerical treatment of nanofluid flow squeezing between two circular plates. Evaluation of energy transmission characteristics of non-Newtonian fluid flow in stratified and non-stratified conditions. Bilal et al. [3] conducted the comparative investigation. Prikhodko et al. [23] investigated two-dimensional acoustic tomography employing encoder neural networks. Using an artificial neural network, Hussain et al. [11] evaluated the heat and mass transport of the Casson nanofluidic flow model on a nonlinear slanted expanding sheet. Liu et al. [18] implemented an adaptive activation function to a class of nonlinear Schrodinger equations and utilized a physically informed neural network. Figure 4 displays the working principle of the multilayer perceptron of the ANN model. Figure 5 illustrates a working procedure that comfortably comprehends an artificial neural network.

3.2.4. *Advantages of Artificial Neural Network.* Artificial neural networks offer several advantages for highly accurate predictions, allowing for more reliable modeling of complex fluid behaviors, the capacity for rapid analysis, and detecting medical images that help to identify cancer cells. Additionally, it generates faster forecasts, managing nonlinear systems, significantly reducing the time required for simulations and decision-making. Furthermore, ANNs facilitate robust data-driven modeling, harnessing vast amounts of data to uncover intricate patterns and relationships within fluid dynamics.

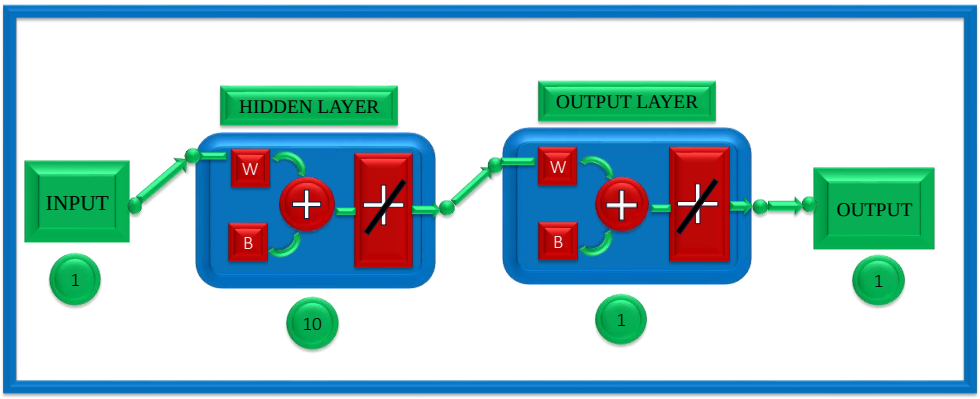

FIGURE 4. ANN multilayer model.

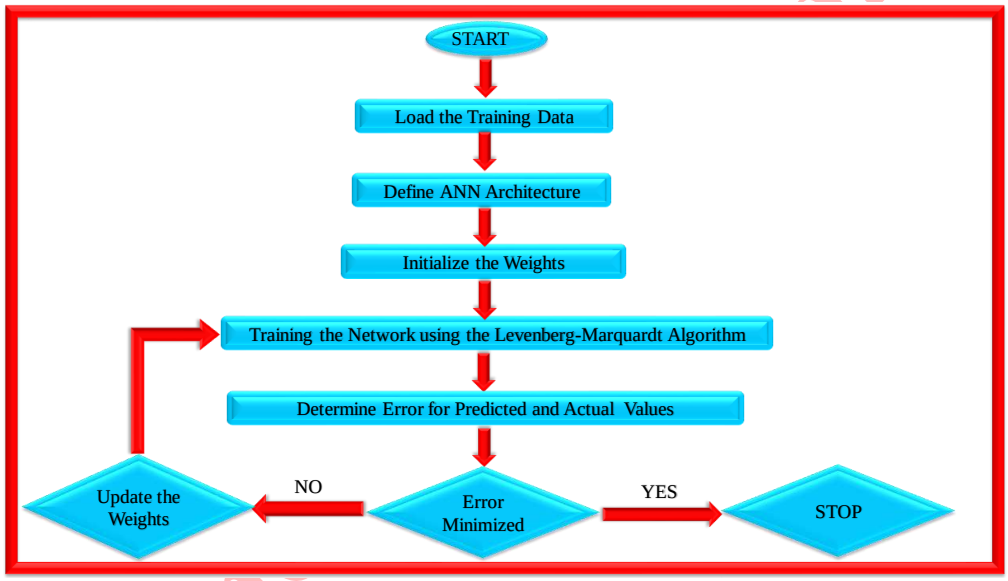

FIGURE 5. ANN prediction algorithm.

4. Results and Discussion

This section highlights several factors that determine the thickness of the temperature, concentration, and velocity profiles. The BVP4C solver in the MATLAB module occupies Equations (2.8)–(2.11) to analyze velocity, temperature, concentration distribution, and non-dimensional physical terms such as Nusselt number, Sherwood number, and skin friction. In machine learning, multiple linear regression also improves accuracy and eliminates errors. Finally, to improve prediction and validation for implementing the artificial neural network model.

4.1. **Impact of Velocity profile.**

Figure 6 illustrates the momentum distribution under different physical parameters and analyzes changes in the fluid motion rates. The velocity profile declined as the magnetic field parameter M developed because a magnetic field interacts with the fluid motion and produces an electromagnetic force. This force, known as the Lorentz force, operates against the direction of flow, slowing it down. Since increased suction restricts the creation of the boundary layer by continuously drawing fluid inward, the velocity distribution decreased when

the suction parameter fw increased. A thinner boundary layer indicates less velocity at the surface, resulting in a slower momentum distribution. Permeability is the loss of energy generated by friction and dispersion within a porous material. Therefore, higher permeability promotes lower fluid motion and minimizes the speed. The momentum of the fluid decreased as the velocity slip condition increased. Higher slip indicates lower resistance at the boundary, resulting in less momentum exchange between the solid surface and the fluid. Since the fluid at the border travels more slowly, it leads to inferior mobility.

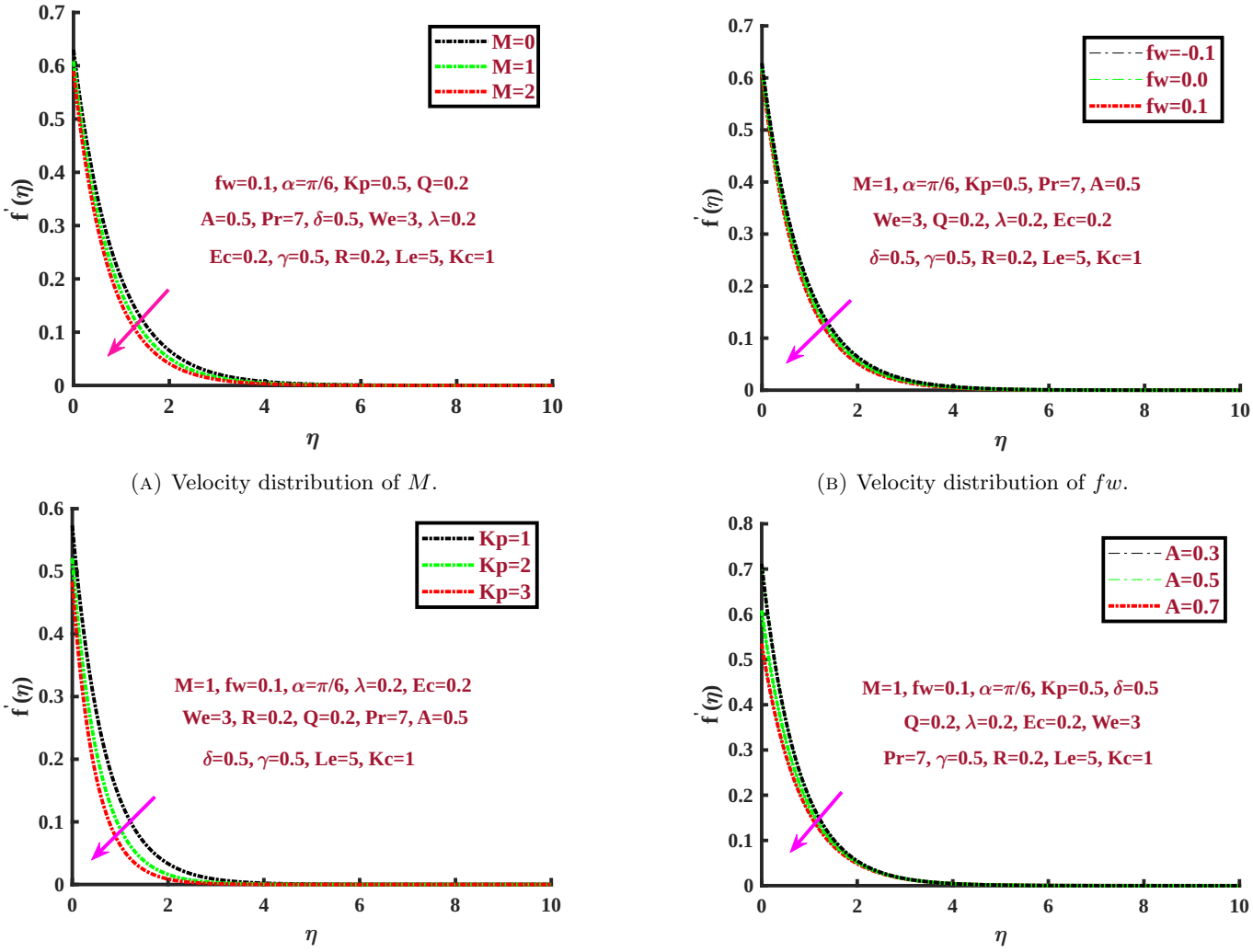

(A) Velocity distribution of M.

(B) Velocity distribution of fw.

(C) Velocity distribution of Kp.

(D) Velocity distribution of A.

FIGURE 6. Several parameters of velocity distribution.

4.2. **Impact of temperature profile.** Figure 7 reveals that variations in fluid temperature affect the fluid behaviors of the physical nature. The temperature profile declined as the Prandtl number Pr rose due to heat transfer primarily occurring through convection rather than conduction. This results in a narrower thermal boundary layer and a more significant decrease in temperature. The temperature profile dropped as the Weissenberg number We expanded due to fluid elastic forces that restricted convective heat transmission. This elasticity specifies the effectiveness of heat diffusion, resulting in a lessened temperature profile. Developing thermal slip δ weakened the thermal

connection, resulting in a lower temperature profile. The thermal boundary layer is thin since fluid retains less heat at the surface.

The temperature profile improves as the Eckert number Ec rises due to viscous forces producing heat as the fluid motion, resulting in higher internal heat production and raising the temperature profile. Thermal radiation R facilitates heat transmission and radiation, therefore enhancing heat transfer. Radiation enables efficient energy emission and absorption, which contributes considerably to accelerating the temperature distribution. The thermal distribution expanded when the heat source parameter Q grew because thermal radiation R improves heat transport and radiation, resulting in higher heat transfer. The heat source parameter Q describes more heat created inside, which raises the temperature profile.

4.3. **Impact of concentration profile.** Figure 8 displays the behaviors for the concentration distribution of Williamson fluid flow in a porous medium. The concentration profile fell as the chemical reaction parameter grew. Superior reaction rates encourage faster chemical transformations, resulting in a higher rate of species diffusion away from reaction zones due to a dilution effect that lowers the presence of reactants in the system. The greater values of Le correspond to the inferior concentration distribution because the higher values of the Lewis number generate less mass diffusion rate since reactant particles diffuse more slowly in the medium. Hence, the intensity of the fluid dropped. Slip effects reduce species diffusion over the boundary layer, resulting in lower concentration profiles for higher γ values. This results in less mixing and lower concentrations across the domain.

4.4. **Impact of skin friction.** The impact of magnetic parameter M, Suction injection parameter fw, Permeability factor Kp, and velocity slip A on skin friction is mentioned in Table 3. The advancement of the skin friction coefficient is the improvement of the magnetic parameter M, the suction injection parameter fw, and the permeability factor Kp. The magnetic field interacts with fluid particles at the surface, causing a thicker boundary layer and increased shear stress at the wall. A maximum velocity slip A causes the fluid to move faster over the surface, decreasing shear stress and skin friction.

TABLE 3. Skin friction $\sqrt{Re_x}C_{f_x}$ effects of several parameters.

M	fw	Kp	A	**Skin friction**
1.0	0.1	0.1	0.1	1.0209
1.5	0.1	0.1	0.1	1.0610
2.0	0.1	0.1	0.1	1.0990
2.5	0.1	0.1	0.1	1.1351
3.0	0.1	0.1	0.1	1.1695
1.0	0.2	0.1	0.1	1.0608
1.0	0.3	0.1	0.1	1.1020
1.0	0.4	0.1	0.1	1.1444
1.0	0.5	0.1	0.1	1.1880
1.0	0.1	0.2	0.1	1.0532
1.0	0.1	0.3	0.1	1.0840
1.0	0.1	0.4	0.1	1.1136
1.0	0.1	0.5	0.1	1.1421
1.0	0.1	0.1	0.2	0.9007
1.0	0.1	0.1	0.3	0.8086
1.0	0.1	0.1	0.4	0.7354
1.0	0.1	0.1	0.5	0.6754

4.5. **Impact of Nusselt number.** Table 4 presents the Nusselt number impact of Prandtl number Pr, Ecklet number Ec, Weissenberg number We, Heat source parameter Q, Radiation factor R, and thermal slip Parameter δ. Higher

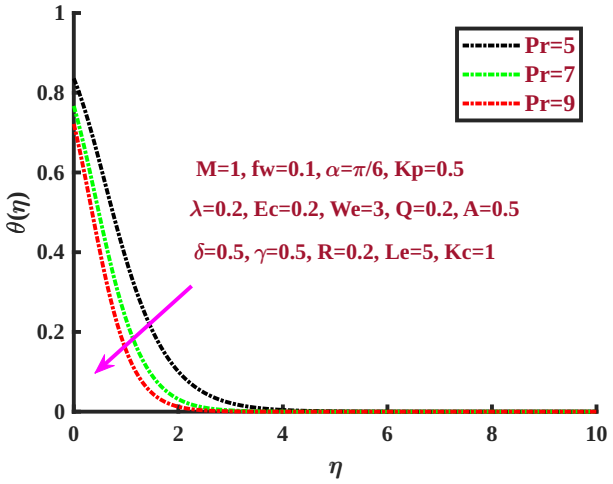

(A) Temperature distribution of Pr.

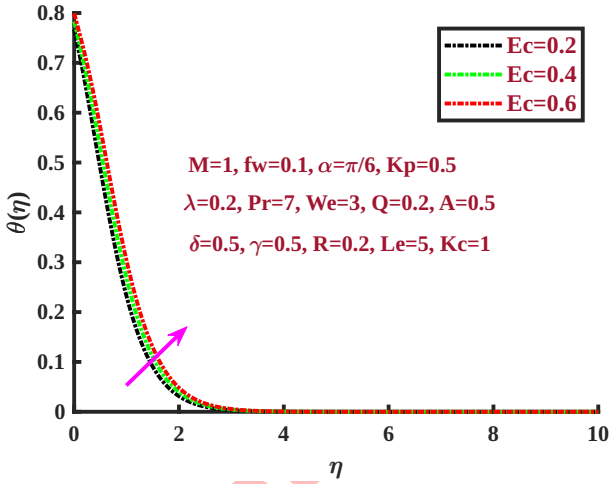

(B) Temperature distribution of Ec.

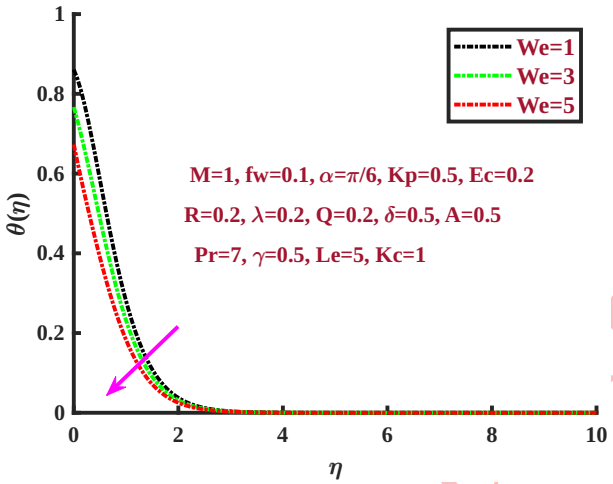

(C) Temperature distribution of We.

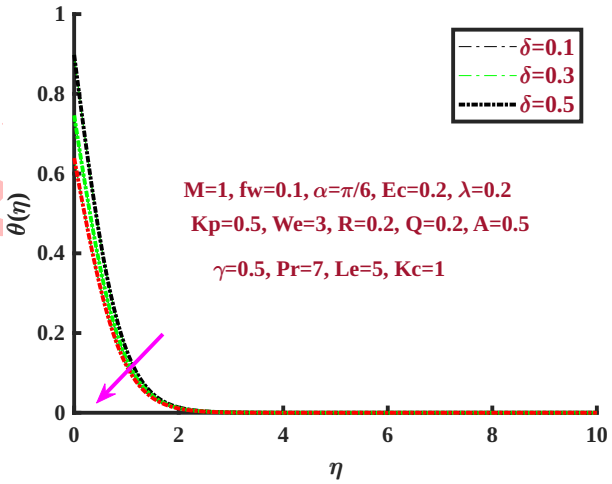

(D) Temperature distribution of δ.

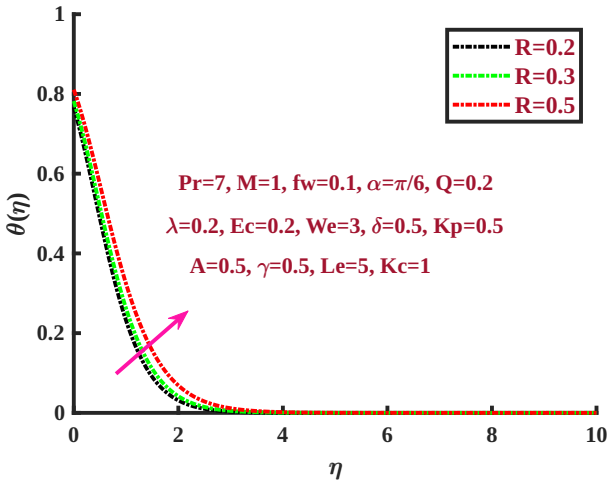

(E) Temperature distribution of R.

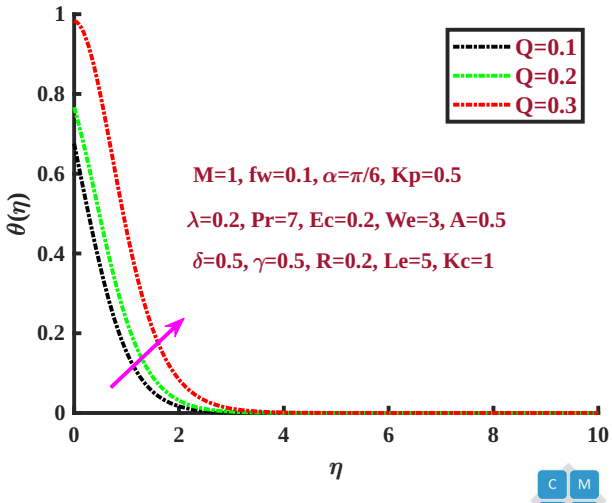

(F) Temperature distribution of Q.

FIGURE 7. Several parameters of temperature distribution.

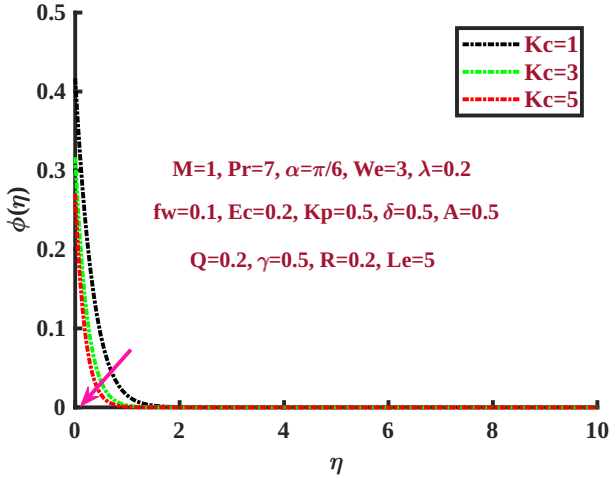

(A) Concentration distribution of Kc.

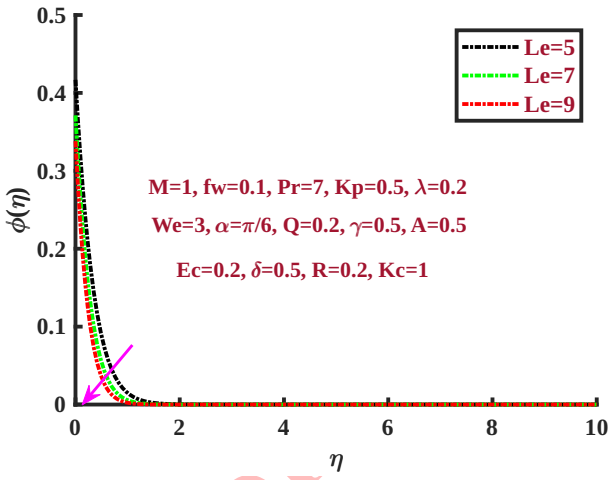

(B) Concentration distribution of Le.

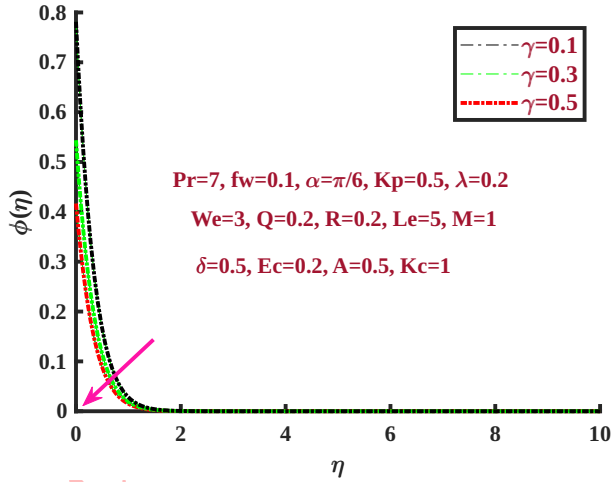

(C) Concentration distribution of γ.

FIGURE 8. Several parameters of concentration distribution.

values of Prandtl number Pr and Weissenberg number We suggest better momentum transmission from the walls due to wall shear stress and elastic effects.

Larger values of heat source parameter Q, Ecklet number Ec, thermal slip Parameter δ, and radiation factor R declined the Nusselt number means the reduction of the temperature deviation in the fluid and the surface, reducing the temperature differential between the fluid and its outermost layer, more heat generation inside the fluid, the slow convective heat transmission for an insulator, and a thicker thermal boundary layer.

4.6. **Impact of Sherwood number.** Table 5 demonstrated the Sherwood number influence for Lewis number Le, Chemical reaction parameter Kc, and concentration slip γ. The Sherwood number value increased for the higher values of the Lewis number (Le) and chemical reaction parameter (Kc) due to enhanced mass transfer accuracy through convection and diffusion. But the concentration boundary layer thickness near the wall reduced as the expansion in concentration slip γ dropped in the Sherwood number.

TABLE 4. Nusselt number $\frac{N_{u_x}}{\sqrt{Re_x}}$ effects of several parameters.

Pr	Ec	We	Q	R	δ	**Nusselt number**
3	0.2	1	0.2	0.2	0.1	0.6734
4	0.2	1	0.2	0.2	0.1	0.8416
5	0.2	1	0.2	0.2	0.1	0.9824
6	0.2	1	0.2	0.2	0.1	1.1053
7	0.2	1	0.2	0.2	0.1	1.2154
3	0.3	1	0.2	0.2	0.1	0.5573
3	0.4	1	0.2	0.2	0.1	0.4411
3	0.5	1	0.2	0.2	0.1	0.3250
3	0.6	1	0.2	0.2	0.1	0.2089
3	0.2	2	0.2	0.2	0.1	0.8455
3	0.2	3	0.2	0.2	0.1	1.0176
3	0.2	4	0.2	0.2	0.1	1.1897
3	0.2	5	0.2	0.2	0.1	1.3618
3	0.2	1	0.3	0.2	0.1	0.4265
3	0.2	1	0.4	0.2	0.1	0.0054
3	0.2	1	0.2	0.3	0.1	0.6288
3	0.2	1	0.2	0.4	0.1	0.5880
3	0.2	1	0.2	0.2	0.2	0.6262
3	0.2	1	0.2	0.2	0.3	0.5851
3	0.2	1	0.2	0.2	0.4	0.5491
3	0.2	1	0.2	0.2	0.5	0.5173

TABLE 5. Sherwood number $\frac{S_{h_x}}{\sqrt{Re_x}}$ effects of several parameters.

Le	Kc	γ	**Sherwood number**
5	1	0.1	2.1866
6	1	0.1	2.3681
7	1	0.1	2.5306
8	1	0.1	2.6781
9	1	0.1	2.8136
5	2	0.1	2.6692
5	3	0.1	3.0131
5	4	0.1	3.2831
5	5	0.1	3.5061
5	1	0.2	1.7942
5	1	0.3	1.5213
5	1	0.4	1.3204
5	1	0.5	1.1664

4.7. **Machine Learning under MLR.** The novel aspect of the multiple linear regression is that it advances the physical quantities for forecasting to a 95% accuracy level. The standardized errors for the physical natures of Sherwood number, Nusselt number, and skin frictions are $2.55E-02$, $5.00E-03$, $3.08E-03$, provided in Tables 6–8. The superior fitting of multiple linear regression makes this standard error approximately equal to zero.

TABLE 6. Skin friction effects of MLR table for actual and anticipated values.

M	fw	Kp	A	**Actual Values**	**Anticipated Values**
1.0	0.1	0.1	0.1	1.0209	1.0121
1.5	0.1	0.1	0.1	1.0610	1.0528
2.0	0.1	0.1	0.1	1.0990	1.0935
2.5	0.1	0.1	0.1	1.1351	1.1342
3.0	0.1	0.1	0.1	1.1695	1.1750
1.0	0.2	0.1	0.1	1.0608	1.0564
1.0	0.3	0.1	0.1	1.1020	1.1007
1.0	0.4	0.1	0.1	1.1444	1.1450
1.0	0.5	0.1	0.1	1.1880	1.1893
1.0	0.1	0.2	0.1	1.0532	1.0457
1.0	0.1	0.3	0.1	1.0840	1.0794
1.0	0.1	0.4	0.1	1.1136	1.1130
1.0	0.1	0.5	0.1	1.1421	1.1467
1.0	0.1	0.1	0.2	0.9007	0.9222
1.0	0.1	0.1	0.3	0.8086	0.8324
1.0	0.1	0.1	0.4	0.7354	0.7426
1.0	0.1	0.1	0.5	0.6754	0.6527

TABLE 7. Nusselt number effects of MLR table for actual and anticipated values.

Pr	Ec	We	Q	R	δ	**Actual Values**	**Anticipated Values**
3	0.2	1	0.2	0.2	0.1	0.6734	0.6880
4	0.2	1	0.2	0.2	0.1	0.8416	0.8248
5	0.2	1	0.2	0.2	0.1	0.9824	0.9616
6	0.2	1	0.2	0.2	0.1	1.1053	1.0983
7	0.2	1	0.2	0.2	0.1	1.2154	1.2351
3	0.3	1	0.2	0.2	0.1	0.5573	0.5670
3	0.4	1	0.2	0.2	0.1	0.4411	0.4460
3	0.5	1	0.2	0.2	0.1	0.3250	0.3250
3	0.6	1	0.2	0.2	0.1	0.2089	0.2040
3	0.2	2	0.2	0.2	0.1	0.8455	0.8552
3	0.2	3	0.2	0.2	0.1	1.0176	1.0225
3	0.2	4	0.2	0.2	0.1	1.1897	1.1897
3	0.2	5	0.2	0.2	0.1	1.3618	1.3569
3	0.2	1	0.3	0.2	0.1	0.4265	0.3626
3	0.2	1	0.4	0.2	0.1	0.0054	0.0373
3	0.2	1	0.2	0.3	0.1	0.6288	0.6362
3	0.2	1	0.2	0.4	0.1	0.5880	0.5843
3	0.2	1	0.2	0.2	0.2	0.6262	0.6424
3	0.2	1	0.2	0.2	0.3	0.5851	0.5968
3	0.2	1	0.2	0.2	0.4	0.5491	0.5513
3	0.2	1	0.2	0.2	0.5	0.5173	0.5057

TABLE 8. Sherwood number effects of MLR table for actual and anticipated values.

Le	Kc	γ	**Actual Values**	**Anticipated Values**
5	1	0.1	2.1866	2.2001
6	1	0.1	2.3681	2.3573
7	1	0.1	2.5306	2.5145
8	1	0.1	2.6781	2.6717
9	1	0.1	2.8136	2.8289
5	2	0.1	2.6692	2.5524
5	3	0.1	3.0131	2.9046
5	4	0.1	3.2831	3.2569
5	5	0.1	3.5061	3.6091
5	1	0.2	1.7942	1.9155
5	1	0.3	1.5213	1.6309
5	1	0.4	1.3204	1.3463
5	1	0.5	1.1664	1.0617

4.8. **Machine Learning under ANN.** Figures 9–13 displayed that machine learning under the ANN model for the training state, performance analysis, error histogram, regression and function fit plots for the numerical and MLR predicted values of skin friction, Nusselt number, and Sherwood number frequencies for testing (15%), validation (15%), and training (70%). After gathering several samples, compress the data, use the model to predict the outcome of every sample, and compare the final results with the desired or actual values.

Figure 9 clarifies the training state graph of the ANN model, which provides the gradient, mu, validation check, and optimal epochs. A mean-squared error (MSE) represents the model convergence. The gradient value indicates that the mathematical model's goal function has attained its lowest local minimum. An estimated Mu gradient is typically zero, indicating a substantial convergence rate.

Validation performance charts displayed in Figure 10 explores the model on the dataset and modifies the network weights at the end of each epoch. MSEs are highest at the beginning of training but decrease as the model approaches optimal conditions. The dotted line indicates the best validation performance.

The steps involved in computing errors are sorting into 20 bins and creating a histogram that plots each of the 20 bins against the total number of samples that contain errors. The X-axis depicts the error bins, while the Y-axis shows the sample that controls the error. The bar diagram demonstrates that the maximum of the data contains zero errors, consistent with the training data employing the Levenberg-Marquardt Scheme. Furthermore, a fundamental tolerance for zero error ensures efficient data training with LMS, as seen in Figure 11.

Figure 12 exhibited the linear regression graphs provided by applying the ANN model to all data-generated predictions using LMS and employing the method to construct linear correlations between targets and outputs. The output formula is Output = R*target + bias. The R-value approximately equal to 1 is displayed in the regression plot, indicating that every ANN is functioning precisely.

In addition, Figure 13 demonstrates that the regulating parameter (Mu) significantly impacts the error convergence. It is further examined and controls the training process of the ANN model. The output is almost equal to the target, considering bias fluctuations. As a result, it concluded that ANNs produce excellent regression analysis results.

5. VALIDATION

5.1. **Validation for Numerical results.** Table 9 portrayed the values of $-\theta^{'}(0)$, resulting in the temperature at the wall, capturing originally found by Wang et al. [42], Gorla et al. [8], Khan et al. [14], Srinu et al. [36] established visualizations for indicating that the non-dimensional variables have an impact on momentum, heat, and mass. Figure 14 displays the results of the numerical simulations, comparing both previous and current outcomes.

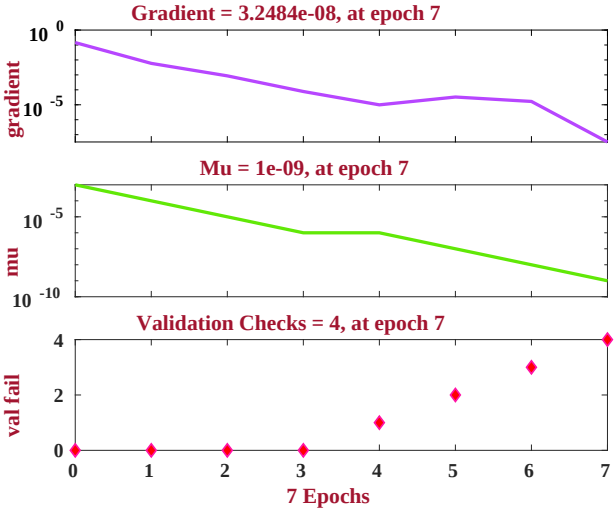

(A) C_{f_x} training state.

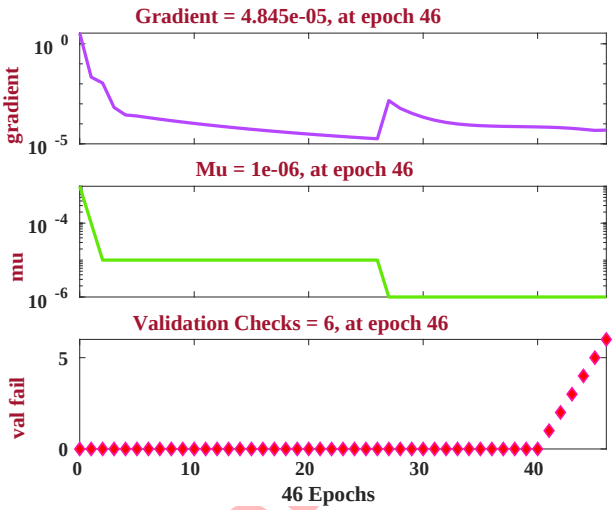

(B) N_{u_x} training state.

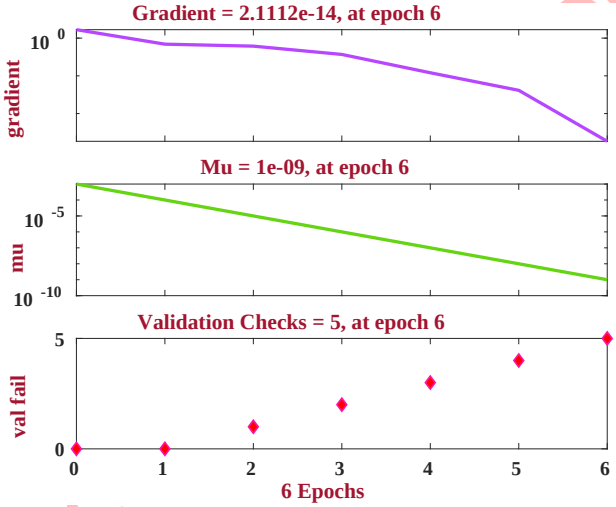

(C) S_{h_x} training state.

FIGURE 9. ANN training state for C_{f_x}, N_{u_x}, S_{h_x}.

TABLE 9. Comparison for $-\theta'(0)$ impacts of Pr values when all parameters are zero.

Pr	Wang et al. [42]	Gorla et al. [8]	Khan et al. [14]	Srinu et al. [36]	Present Result
0.7	0.4539	0.4539	0.4539	0.4539	0.4544
2	0.9113	0.9114	0.9114	0.9113	0.9114
7	1.8954	1.8905	1.8954	1.8954	1.8954

5.2. **Validation for Multiple Linear Regression results.** Table 10 highlighted the level of precision dependency of the multiple linear regression model. The values of R^2 and adjusted R^2 are approximately equal to 1, even though the standard and root mean square errors are negligible. It emphasizes an appropriate fitting level for multiple linear regression.

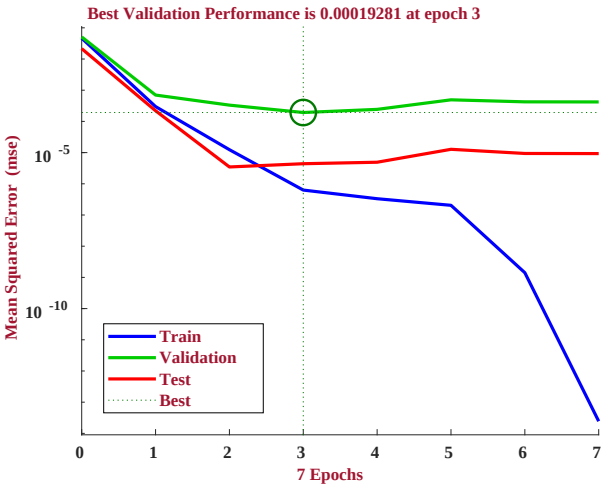

(A) C_{f_x} performance.

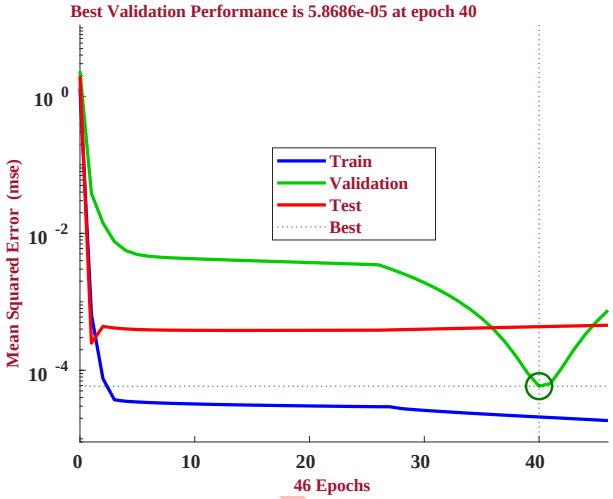

(B) N_{u_x} performance.

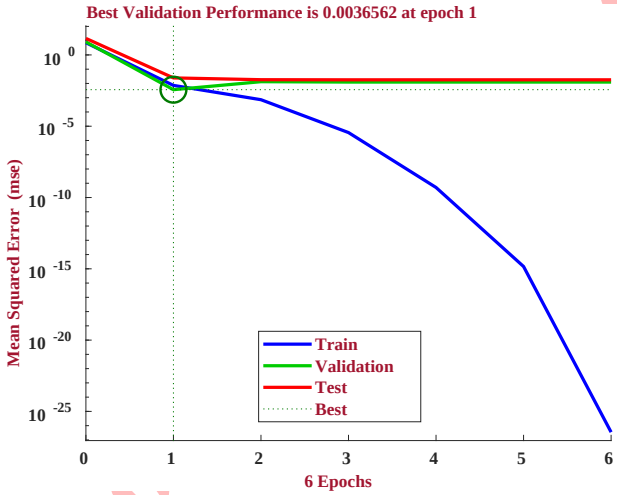

(C) S_{h_x} performance.

FIGURE 10. ANN performance for C_{f_x}, N_{u_x}, S_{h_x}.

TABLE 10. MLR statistics for C_{f_x}, N_{u_x}, and S_{h_x}.

Statistics	SE	R-square	Observations	Adjusted R Square	RMSE
MLR C_{f_x}	3.08E-03	0.995	17	0.993	0.0127
MLR N_{u_x}	5.00E-03	0.997	21	0.996	0.0229
MLR S_{h_x}	2.55E-02	0.988	13	0.985	0.0918

5.3. **Validation for Artificial Neural Network results.** Table 11 represents the ANN Statistics for Skin friction, Nusselt number, and Sherwood number. ANN delivers great regression analysis results when the MSE, gradient, and performance values are modest and the number of epochs increases.

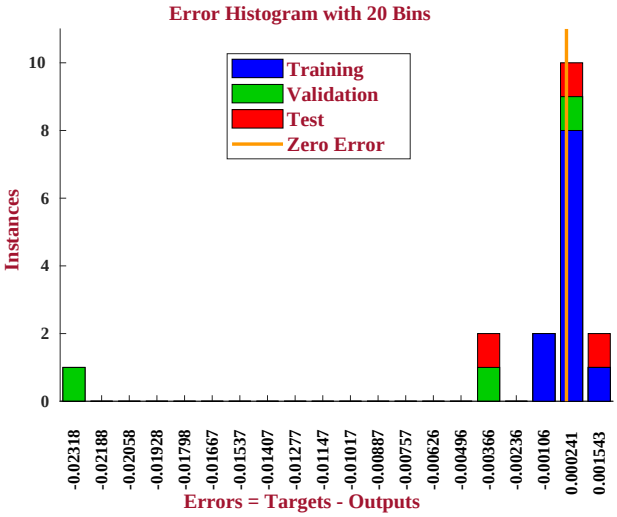

(A) C_{f_x} error histogram.

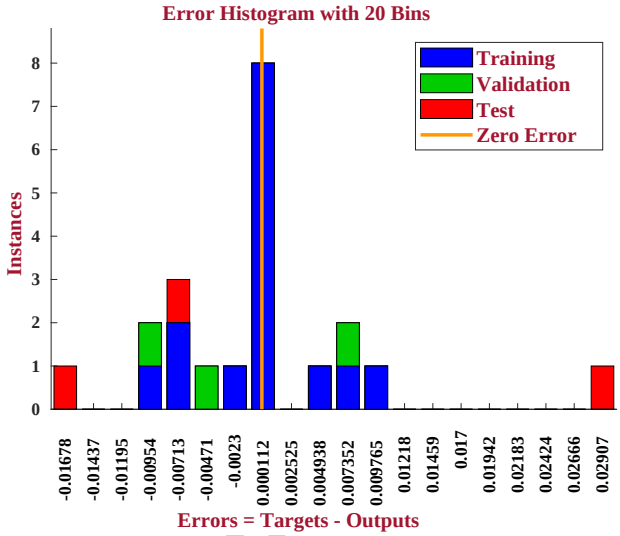

(B) N_{u_x} error histogram.

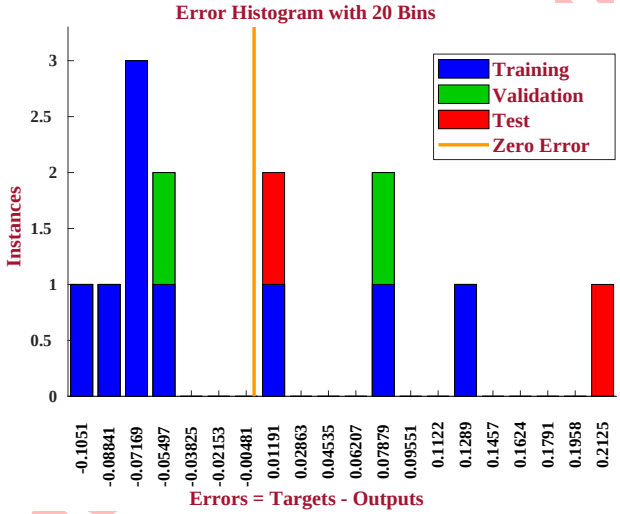

(C) S_{h_x} error histogram.

FIGURE 11. ANN error histogram for C_{f_x}, N_{u_x}, S_{h_x}.

TABLE 11. ANN statistics for C_{f_x}, N_{u_x}, and S_{h_x}.

Statistics	Train	Test	Validation	Epochs	Grad	Performance	Mu
ANN C_{f_x}	6.2972E-07	4.4035E-06	1.9281E-04	7	3.25E-08	2.45E-14	1.00E-09
ANN N_{u_x}	2.0843E-05	4.3355E-04	5.8686E-05	46	4.85E-05	1.85E-05	1.00E-06
ANN S_{h_x}	7.3000E-03	2.4400E-02	3.7000E-03	6	2.11E-14	3.50E-27	1.00E-09

6. Concluding Remarks

The current work investigates the flow of a Williamson fluid over an inclined sheet driven by a magnetic field and radiation under the effects of velocity, temperature, and concentration slips. Notable outcomes include the following:

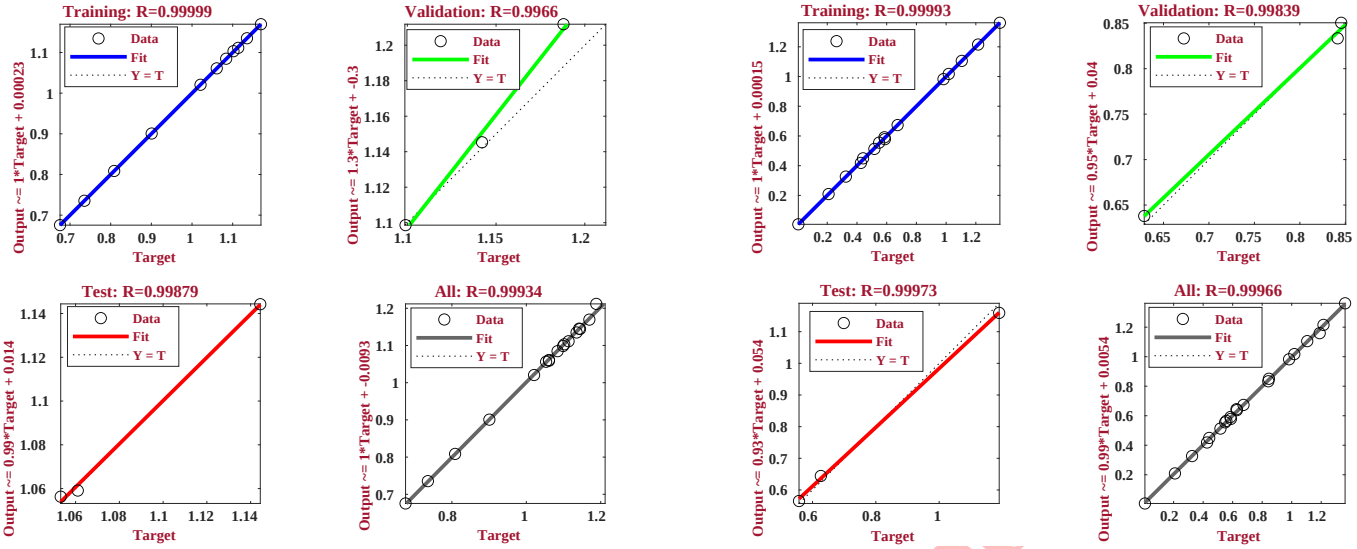

(A) C_{f_x} regression. (B) N_{u_x} regression.

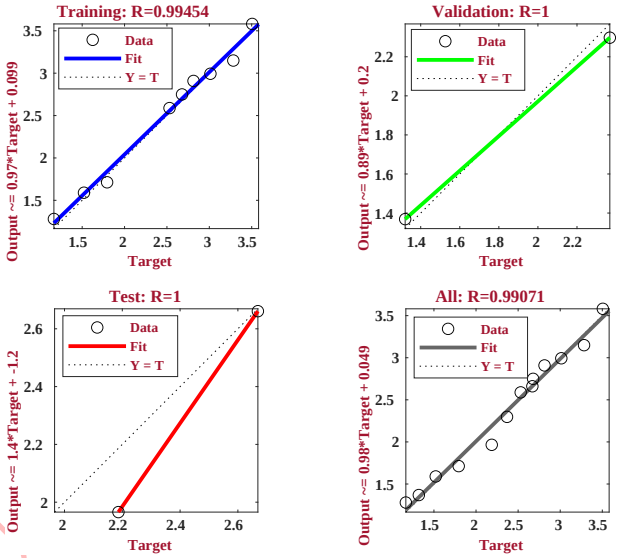

(C) S_{h_x} regression.

FIGURE 12. ANN regression for C_{f_x}, N_{u_x}, S_{h_x}.

- The larger values of the magnetic parameter and velocity slip reduced the velocity distribution for the Lorentz force developed for the magnetic field changes and lowered the boundary layer surface.
- The temperature profile dropped for the Weissenberg and Prandtl numbers expands because the temperature boundary layer thins and reduces heat transfers from the fluid to the surface.
- Multiple regression strategies used in the machine learning methodology yielded good fitting MLR catches with R^2 values about equivalent to 1 and achieved a 95% accuracy between predicted and actual attainments.

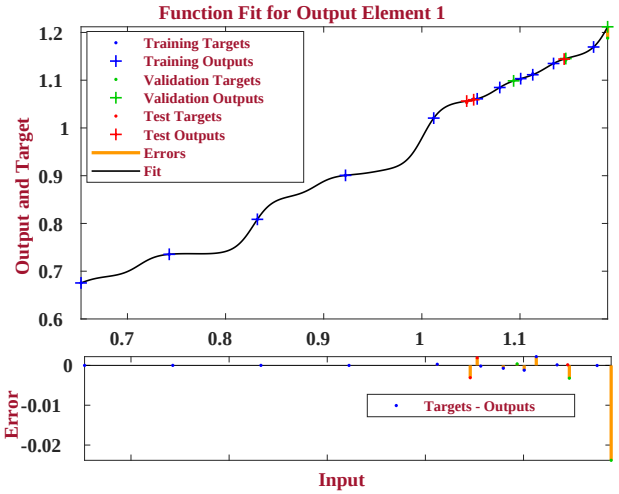

(A) C_{f_x} function fit.

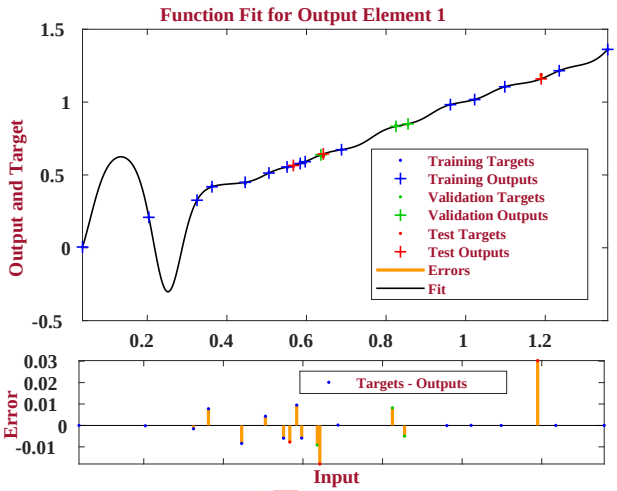

(B) N_{u_x} function fit.

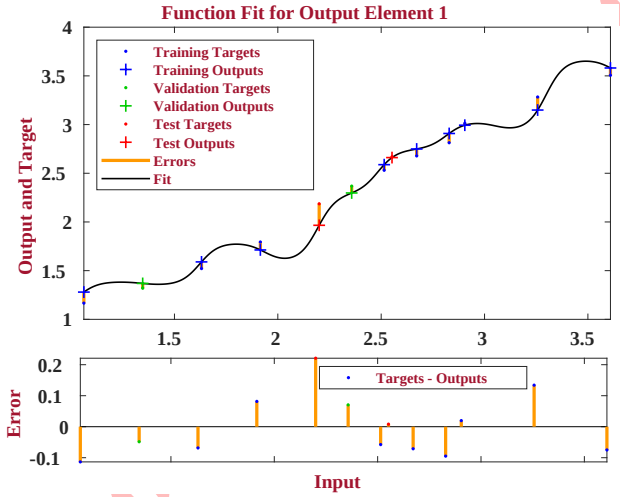

(C) S_{h_x} function fit.

FIGURE 13. ANN function fit for C_{f_x}, N_{u_x}, S_{h_x}.

- The execution of the artificial neural network model confirms the multilayer perceptron's predicted and numerical values for the physical parameters. The mean square error, gradient, and performance values are negligible, and an elevated number of epochs indicates a perfect regression analysis with 99% validity.
- The biological application of permeability ideas involves the creation of porous scaffolds for tissue engineering, hyperthermia for cancer treatment, drug delivery systems, and blood circulation. Future researchers can explore the change in velocity, temperature, and concentration in the physical characteristics of the Williamson fluid.
- Further research on Williamson fluid and thermal energy radiation is needed to evaluate the effectiveness and improve prediction abilities. It looks into several potential directions for implementing an artificial neural network algorithm.

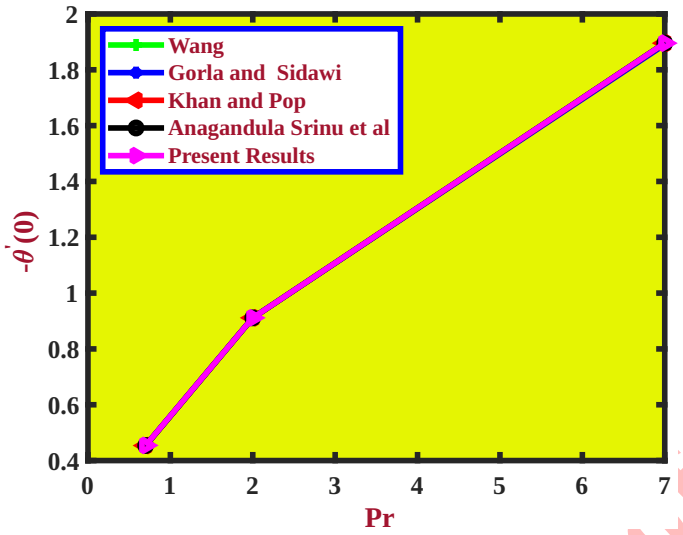

FIGURE 14. Comparison of previous and present numerical outcomes.

NOMENCLATURE

A	Velocity slip ($A = A^* \sqrt{\frac{a}{\nu}}$)
δ	Thermal slip ($\delta = B^* \sqrt{\frac{a}{\nu}}$)
γ	Concentration slip ($\gamma = C^* \sqrt{\frac{a}{\nu}}$)
v_0	Suction velocity constant
B_0	Magnetic field coefficient
u^* and v^*	Component of velocity along the x and y axes (M/S)
k^*	Permeability of a porous medium
α	Angle of inclination factor
K_p	Permeability factor
T^*	Temperature of the fluid (K)
T_w	The temperature of the wall (K)
T_∞	Ambient temperature (K)
C^*	Concentration of the fluid
C_w	The fluid concentration at the plate
C_∞	Ambient concentration
ρ	Fluid density(Kg/M^2)
k	Fluid magnetic permeability
ν	Kinematic viscosity (M^2/S)
Q	The parameter of heat source

DATA AVAILABILITY STATEMENT

The data that support the findings of this paper are available from the corresponding author upon reasonable request.

ACKNOWLEDGMENT

The authors are very grateful to the reviewers for carefully reading the paper and for their comments and suggestions, which have improved the paper.

Conflicts of Interest

The authors declare no conflict of interest.

References

[1] M. A. Abdelhafez, A. M. Abd-Alla, S. M. Abo-Dahab, and Y. Elmhedy, *Influence of an inclined magnetic field and heat and mass transfer on the peristaltic flow of blood in an asymmetric channel.*, Sci. Rep., *13*, (5749) (2023).

[2] M. M. Bhatti, and M. M. Rashidi, *Effects of thermo-diffusion and thermal radiation on Williamson nanofluid over a porous shrinking/stretching sheet*, J. Mol. Liq., *221* (2016), 567-573.

[3] S. Bilal, Asadullah, and M.B. Riaz, *Evaluating Energy Transmission Characteristics of Non-Newtonian Fluid Flow in Stratified and non-Stratified Regimes: A Comparative Study*, Results in Engineering, (2024).

[4] Shikha Chandel and Shilpa Sood, *Numerical analysis of Williamson-micropolar nanofluid flow through the porous rotatory surface with slip boundary conditions*, Int. J. Appl. Comput. Math., *8*(134) (2022).

[5] R. Choudhari, *Analysis of multiple slip effects on MHD blood peristaltic flow of Phan–Tien–Tanner nanofluid through an asymmetric channel*, Int. J. Modern Phys. BVol., *37*(11) (2023), 2350102.

[6] D. Dey and B. Chutia, *Two-phase fluid motion through porous medium with volume fraction: An application of MATLAB bvp4c solver technique*. Heat Transfer., (2021), 1-12.

[7] N. S. Elgazery, *Nanofluids flow over a permeability unsteady stretching surface with a non-uniform heat source/sink in the presence of the inclined magnetic field*, J Egypt Math Soc 27., *9* (2019).

[8] R. S. Reddy Gorla, and I. Sidawi, *Free convection on a vertical stretching surface with suction and blowing*, Appl Sci Res., *52* (1994), 247–257.

[9] I. Haider, U. Nazir, M. Nawaz, S. O. Alharbi, and I. Khan, *Numerical thermal study on the performance of hybrid nano-Williamson fluid with memory effects using novel heat flux model*, Case Stud. Therm. Eng., *26* (2021), 101070.

[10] A. Heureux, K. Grolinger, H. F. Elyamany, and M. A. M. Capretz, *Machine Learning with Big Data: Challenges and Approaches*, IEEE Access, *5* (2017), 7776–7797.

[11] S. Hussain. Islam, M. A. Z. Raja, K. S. Nisar, and M. Shoaib, *Intelligent computing technique to study heat and mass transport of Casson nanofluid flow model on a nonlinear slanted extending sheet*, Journal of Applied Mathematics and Mechanics, *104* (2024), e202300224.

[12] Aleya Ashima Mohd Kamil, and Fazlina Aman, *Solving Thermal Radiation On Boundary Layer Flow Using BVP4C Technique*, Enhanced Knowledge in Sciences and Technology *2*(1) (2022), 048-055.

[13] W. A. Khan, J. R. Culham, and O. D. Makinde, *Combined heat and mass transfer of third-grade nanofluids over a convectively heated stretching permeable surface*, Can. J. Chem. Eng., *93*(10) (2015), 1880–1888.

[14] W. A. Khan and I. Pop, *Boundary-layer flow of a nanofluid past a stretching sheet*, Int J Heat Mass Transf., *53*(11–12) (2010), 2477–2483.

[15] M. Khan, M. Y. Malik, T. Salahuddin, and A. Hussian, *Heat and mass transfer of Williamson nanofluid flow yield by an inclined Lorentz force over a nonlinear stretching sheet*, Result Phys., *8* (2018), 862–868.

[16] O. K. Koriko, N. A. Shah, S. Saleem, J. D. Chung, A. J. Omowaye, and T. Oreyeni, *Exploration of bioconvection flow of MHD thixotropic nanofluid past a vertical surface coexisting with both nanoparticles and gyrotactic microorganisms*, Scientific reports, *11*(1) (2021), 16627.

[17] M. V. Krishna and A. J. Chamkha, *Hall and ion slip effects on MHD rotating flow of elastic-viscous fluid through a porous medium*, Int. Commun. Heat Mass Tran, *113*, (2020), 104494.

[18] S. Liu, Z. Luan, S. I. Kabanikhin, S. V. Strijhak, and Y. Zhang, *Solving a type of nonlinear schro Dinger equations using a physically informed neural network and tuning the adaptive activation function*. TWMS Journal of Pure and Applied Mathematics, *15*(2) (2024), 203-227.

[19] D. V. Lyubimov and A. V. Perminov, *Motion of a thin oblique layer of a pseudo-plastic fluid*, J. Eng. Phys. Thermophys., *75*(4) (2002), 920-924.

[20] S. Nadeem, S. T. Hussain, and Changhoon Lee, *Flow of a Williamson fluid over a stretching sheet*, Braz. J. Chem. Eng., *30*(3) (2013), 619–625.

[21] S. Palash, K. R. Parameshwaran, S. Sandip, and Deshmukh, *Thermal conductivity prediction of titania-water nanofluid: A case study using different machine learning algorithms*, Case Studies in Thermal Engineering, *30* (2022), 101658.
[22] B. C. Prasannakumar, B. J. Gireesha, S. R. Rama, M. R. Gorla, M. R. Krishnamurthy, *Effect of a chemical reaction and nonlinear thermal radiation on Williamson nanofluid slip flow over a stretching sheet embedded in a porous medium*, J. Aero. Eng., (2015).
[23] A.Y. Prikhodko, M. A. Shishlenin, N. S. Novikov, and D. Klyuchinskiy, *Encoder neural network in 2D acoustic tomography*. Applied and Computational Mathematics, *23*(1) (2024), 83-98.
[24] P. Priyadharshini, and M. Vanitha Archana, *Augmentation of magnetohydrodynamic nanofluid flow through a Permeable stretching sheet employing Machine learning algorithm*, Examples and Counterexamples, *3* (2023), 100093.
[25] P. Priyadharshini, V. Karpagam, Nehad Ali Shah, and Mansoor H. Alshehri, *Bio- Convection effects of MHD Williamson fluid flow over a symmetrically stretching sheet: Machine learning*, MDPI Symmetry, *15*(9) (1684), (2023).
[26] M. Ramamoorthy, and L. Pallavarapu, *Second order slip flow of a conducting Jeffrey nanofluid in an inclined asymmetric porous conduit with heat and mass transfer*, Multidiscip Model Mater Struct., *18*(6) (2022),1016–1038.
[27] K. Ramesh and M. Devakar, *Effect of heat transfer on the peristaltic transport of an MHD second grade fluid through a porous medium in an inclined asymmetric channel*, Chinese. J. Phys. *55*(3) (2017), 825–844.
[28] A. Rauf, Faisal, N. A. Shah, and T. Botmart, *Hall current and morphological effects on MHD micropolar non-Newtonian tri-hybrid nanofluid flow between two parallel surfaces*, Scientific Reports, *12*(1) (2022), 16608.
[29] S. U. Rehman, N. Fatima, B. Ali, M. Imran, L. Ali, N. A. Shah, and J. D. Chung, *The Casson dusty nanofluid: Significance of Darcy–Forchheimer law, magnetic field, and non-Fourier heat flux model subject to stretch surface*, Mathematics, *10*(16) (2022), 2877.
[30] L. F. Shampine, J. Kierzenka, and M. W. Reichelt, *Solving boundary value problems for ordinary differential equations in MATLAB with bvp4c*, Tutorial Notes, (2000), 1–27.
[31] L. F. Shampine, I. Gladwell, and S. Thompson, *Solving ODEs with Matlab*, Cambridge University Press, (2003).
[32] M. D. Shamshuddin, G. R. Rajput, W. Jamshed, F Shahzad, S. O. Salawu, A. Aissa, and V. S. Patil, *MHD bioconvection microorganism nanofluid driven by a stretchable plate through porous media with an induced heat source*, Waves in Random and Complex Media, (2022).
[33] M. Shoaib, M. A. Z. Raja, G. Zubair, I. Farhat, K. S. Nisar, Z. Sabir, and W. Jamshed, *Intelligent computing with Levenberg–Marquardt backpropagation neural networks for third-grade nanofluid over a stretched sheet with convective conditions*, an Arabian journal for science and engineering, (2021), 1-19.
[34] P. Sreedevi, P. S. Reddy, and A. J. Chamkha, *Heat and mass transfer analysis of nanofluid over a linear and nonlinear stretching surface with thermal radiation and chemical reaction*, Powder Technol, *315*, (2017), 194–204.
[35] T. Srinivasulu, and B. S. Goud. *Effect of inclined magnetic field on flow, heat and mass transfer of Williamson nanofluid over a stretching sheet*, Case Stud Therm Eng., *23* (2021), 100819.
[36] Anagandula Srinu, K. Sreeram Reddy, and N. Amar, *Radiation and inclined magnetic field effects on Williamson fluid flow above a stretching sheet in the existence of velocity, thermal, and concentration slips*, Partial Differential Equations in Applied Mathematics, *9* (2024), 100611.
[37] C. Sulochana, T. Kumar, *Regression modeling of hybrid nanofluid flow past an exponentially stretching/shrinking surface with heat source-sink effect*, Materials Today: Proceedings, *54* (2021).
[38] K. Umair, Z. Aurang, A. B. Sakhinah, I. Anuar, B. Dumitru, E. L. Sayed, and M. Sherif, *Computational simulation of cross-flow of Williamson fluid over a porous shrinking/stretching surface comprising hybrid nanofluid and thermal radiation*. AIMS Mathematics, *7*(4) (2022), 6489–6515.
[39] Hakeem Ullah, Mehreen Fiza, Muhammad Asif Zahoor Raja, Imran Khan, Muhammad Shoaib, and M. Seham, *Al-Mekhlaf, Intelligent Computing of Levenberg-Marquard Technique Backpropagation Neural Networks for Numerical Treatment of Squeezing Nanofluid Flow between Two Circular Plates*, Mathematical Problems in Engineering, (2022).

[40] S. Usman, M. B. Shaheen, Arain, Kottakkaran Sooppy Nisar, M. D. Ashwag Albakri, Shamshuddin, and Fouad Othman Mallawi, *A case study of heat transmission in a Williamson fluid flow through a ciliated porous channel: A semi-numerical approach*, Case Studies in Thermal Engineering, *41* (2023), 102523.
[41] C. Vasudev, U. R. Rao, M. V. S. Reddy, and G. P. Rao *Peristaltic Pumping of Williamson fluid through a porous medium in a horizontal channel with heat transfer*, Amer. J. Sci. Ind. Res., *1*(3) (2010), 656–666.
[42] C. Y. Wang, *Free convection on a vertical stretching surface*, ZAMM J Appl Math Mech., *69*(11) (1989), 418–420.
[43] R. V. Williamson, *The flow of pseudo-plastic materials*, Ind. Eng. Chem., *21*(11) (1929).
[44] Dharmendar Reddy Yanala, Vempati Srinivasa Rao, and L. Anand Babu,*MHD boundary layer flow of nanofluid and heat transfer over a nonlinear stretching sheet with chemical reaction and suction/blowing*, Journal of Nano Fluids, *7*(2) (2018), 404–412.